

Sustainable and Green Synthesis of Iron Nanoparticles Supported on Natural Clays via Palm Waste Extract for Catalytic Oxidation of Crocein Orange G Mono Azoic Dye

Dhiss Tesnim,* Ben Amor Hedi, and Jesus Simal-Gandara*



Cite This: *ACS Omega* 2023, 8, 34364–34376



Read Online

ACCESS |

Metrics & More

Article Recommendations



ABSTRACT: In this study, the removal of Crocein Orange G dye (COG) from aqueous solution was investigated using an innovative green catalyst to overcome problems with chemical techniques. Clay bentonite El Hamma (HB)-supported nanoscale zero-valent iron (NZVI) was used as a heterogeneous Fenton-like catalyst for the oxidation of harmful COG. Palm waste extract was herein used as a reducing and capping agent to synthesize NZVI, and HB clay was employed, which was obtained from the El Hamma bentonite deposit in the Gabes province of Tunisia. HB and HB-NZVI were characterized by various techniques such as scanning electron microscopy (SEM), transmission electron microscopy (TEM), Brunauer, Emmett, and Teller (BET), Fourier transform infrared spectroscopy (FTIR), dynamic light scattering (DLS), X-ray diffraction (XRD), and zeta potential. Under optimal conditions, total degradation of COG was attained within 180 min. Kinetic studies showed that the dye degradation rate followed well the pseudo-second-order model. The apparent activation energy was 33.11 kJ/mol, which is typical of a physically controlled reaction. The degradation pathways and mineralization study revealed that the adsorption-Fenton-like reaction was the principal mechanism that demonstrated 100% degradation efficiency of COG even after three successive runs. Obtained results suggest that HB-NZVI is an affective heterogeneous catalyst for the degradation of COG by H_2O_2 and may constitute a sustainable green catalyst for azoic dye removal from industrial wastewaters.

1. INTRODUCTION

The textile industries, specifically coloring operations, are responsible for releasing a considerable amount of color pollutants;¹ these are expanding a significant source of natural contamination.² Indeed, the release of many benzene rings included in the dyes poses a serious threat to the environment.³ Direct dyes, acid dyes, basic dyes, azoic dyes, and disperse dyes are examples of dyes that are carcinogenic. Moreover, dye-contaminated water creates other serious health problems and has a negative impact on the ecosystem even in minute levels.⁴ An estimated 60–70% of colors produced for the textile industry are azo dyes.⁵ The compounds of the azo group are chemically represented as $(\text{R}-\text{N}=\text{N}-\text{R}')$, with $(-\text{N}=\text{N}-)$ being the chromophore group referred to as azo.⁶ The reactive azo dye Crocein Orange G (COG) is a common one and is frequently used to color textiles.⁷ Due to

its toxicity, mutagenicity, and carcinogenicity, the COG dye is a poorly biodegradable pollutant that can cause a severe environmental concern.^{8,9}

The need for a sustainable and safe water is to develop innovative and economical methods for purification and treatment of wastewater. Diverse physical, chemical, biological, and electrochemical processes have been used to treat these pollutants from wastewater.^{10–12} One of the main methods for

Received: February 27, 2023

Accepted: June 5, 2023

Published: September 11, 2023



removing these dyes is catalytic degradation.^{13–15} Advanced oxidation processes (AOPs) are based on the use of radical transition species, such as (HO•) with high reactivity and no selectivity.^{16,17} A hydroxyl radical can change harmful pollutant matters into intermediate substances, which can further cause reactions with other oxidizing agents or these radicals and become mineralized as CO₂, H₂O, and other organic and inorganic minerals.^{18,19} The Fenton process is one of the AOPs that is very efficient in degrading a wide range of azo dyes.^{20–22} It is generally recognized that the homogeneous Fenton process has a number of drawbacks, including the need for additional treatments for sludge and iron ions, the acidity of effluents prior to decontamination, and the neutralization of treated solutions prior to disposal.^{23–26} To address these issues, heterogeneous Fenton oxidation based on various Fe-based catalysts has been developed in the past few years.^{27,28}

Nanoscale zero-valent iron (NZVI) has been used recently in the Fenton heterogeneous system due to its large specific surface area and high reactivity.^{29–32} NZVI is an environmentally friendly material with strong treatment efficiency, controllable particle size (1–100 nm), and abundant activate sites.^{33,34} Iron nanoparticle technology represents perhaps one of first-generation nanoscale environmental technologies.³⁵ NZVI production commonly uses very reactive and toxic reducing agents such as sodium borohydride and hydrazine hydrate, which cause undesired detrimental impacts on the environment and the plant and animal life it supports.³⁶ To overcome this inconvenience, researchers continue efforts to develop facile, effective, and reliable green chemistry processes for the production of nanomaterials.³⁷ Various organisms act as clean, eco-friendly, and sustainable precursors to produce stable and well-functionalized nanoparticles.^{37,38} Plant-mediated approaches are simple, non-toxic, cost-effective, low-cost, and eco-friendly.^{33,39,40} However, similar to other nanomaterials, this ultra-fine powder has a strong tendency to agglomerate into larger particles, resulting in an adverse effect on both effective surface area and catalyst performance, while the separation and recovery of fine NZVI particles after utilization are another disadvantage of this material.^{41–43} Suitable candidates can serve as support materials because they are an abundant natural resource,^{43–45} such as bentonite,^{44,46} kaolin,⁴⁷ biochar,^{31,48} and activated carbon⁴⁹-supported NZVI.

In recent years, a specific focus has been devoted to clay-supported NZVI composite materials for the remediation of contaminated aqueous solutions due to their high removal efficiency and fast degradation rate.^{47,50,51} The synergetic effect between adsorption by the clay mineral and removal by NZVI particles is primarily responsible for the pollutant removal by clay-NZVI composites. In contrast to NZVI particles and neat clay mineral, these composite materials have better removal efficiency.

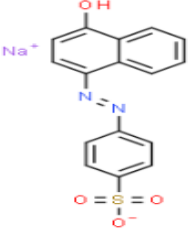
In this work, a green synthesis of NZVI was performed by a novel, easy, and simple method using an abundant and annually renewable palm waste. The extract was obtained using a coffee maker, which differs from conventional methods such as hot extraction,⁵² cold extraction,⁵³ microwave irradiation,⁵⁴ and the use of Soxhlet apparatus,⁵⁵ which were later used in NP synthesis. HB-NZVI, which is applied as a catalyst for the degradation of monoazo dye Crocein Orange G (COG) by hydrogen peroxide (H₂O₂) in aqueous solution, was synthesized using the local bentonite from El Hamma-Gabes deposit (HB) as a support. Batch experiments were undertaken to study the effects of experimental parameters such as initial

pH, initial concentration of COG, dosage of HB-NZVI, and temperature on the removal of COG. Scanning electron microscopy (SEM), transmission electron microscopy (TEM), Brunauer, Emmett, and Teller (BET), Fourier transform infrared spectroscopy (FTIR), dynamic light scattering (DLS), X-ray diffraction (XRD), pH, and zeta potential were used to characterize HB and HB-NZVI.

2. MATERIALS AND METHODS

2.1. Materials. Hydrogen peroxide (30% w/w), hydrochloric acid (36.5% w/w), sodium hydroxide, and ferric chloride hexahydrate (FeCl₃·6H₂O) were of analytical grade and were purchased from Laboratory Chemical. Crocein Orange G dye (COG, also known as acid orange 7) (99%) was provided by Sigma-Aldrich Company. Its principal characteristics are assigned in Table 1.

Table 1. Physical and Chemical Properties of COG Dye

Molecular structure	
Molecular formula	C ₁₆ H ₁₁ N ₂ NaO ₄ S
Molar Mass (g/mol)	350.32
Water solubility (g/L)	1 at 20 °C
pK _{a1} -pK _{a2}	1-10.6
λ _{max} (nm)	495

In aqueous solution, COG may exist under three forms (H₂L, HL⁻, and L²⁻). According to pK_a_i values, the predominant form in the pH range of 2 to 10 is HL⁻.^{56–58}

The clay used in this work was extracted from El Hamma-Gabes deposit (south of Tunisia). Before its use, the natural clay was dried at 80 °C overnight, crushed, and sieved through a series of sieves and the fraction of particles having a size less than 1 mm was recovered and subjected to decantation in water. The purified clay (*d* < 0.22 μm) was recuperated according to Stokes law. The chemical composition of the purified bentonite is depicted in Table 2.

The lignocellulose palm waste (PW) collected from Gabes oasis was first washed with water to remove the dust and adhering impurities, dried in an oven at 80 °C, and then cut into pieces of 1 to 2 mm before storing in an oven until use.

2.2. Methods. **2.2.1. HB-NZVI Catalyst Preparation.** The NZVI nanoparticles were prepared using a similar procedure described in a previous study⁵⁹ with some modifications. The procedure was as follows:

In a beaker, 2.0 g of bentonite (HB) was poured in 100 mL of distilled water and left for 60 min at room temperature under magnetic stirring. At that time, in 100 mL of deionized

Table 2. Chemical Composition of Bentonite Clay

percentage (%)	chemical composition							humidity (by Karl Fisher method)
	SiO ₂	Al ₂ O ₃	Fe ₂ O ₃	SO ₃	MgO	CaO	CO ₂	
	52.07	17.94	6.29	3.07	1.77	0.27	1.49	8.44

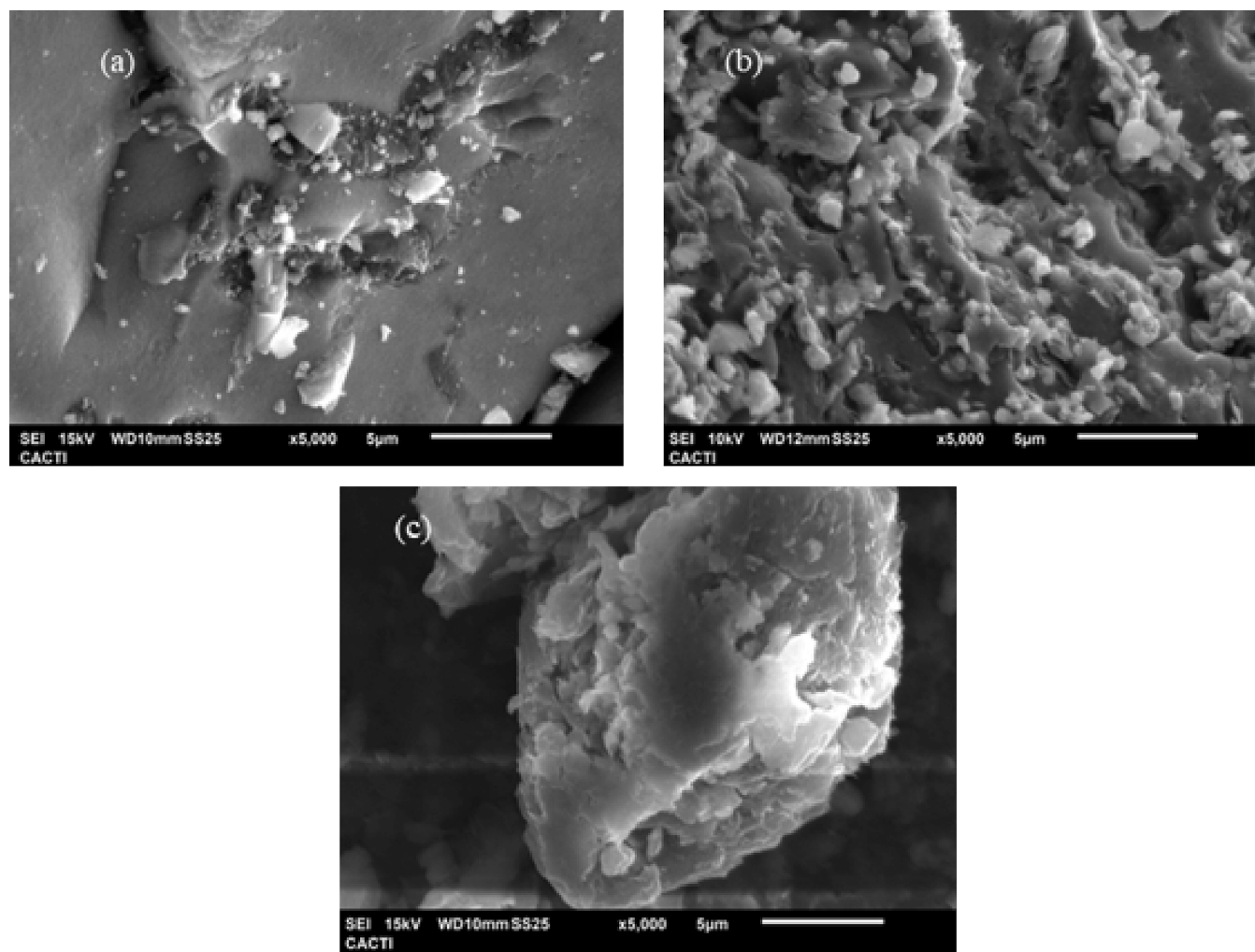
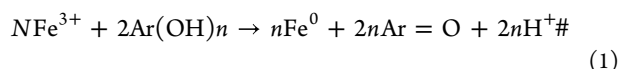


Figure 1. SEM images of NZVI (a), HB-NZVI (b), and HB clay (c).

water, 2.7 g of solid FeCl₃·6H₂O was dissolved to create a 0.10 mol/L FeCl₃·6H₂O solution. Ferric chloride and bentonite suspension (HB) were mixed and agitated continuously for 24 h. After that, the extract of palm waste obtained using a coffee maker was added gradually for 15 min at room temperature. The color of the solution changes from yellow to black after the addition, showing that the iron(III) ions have been converted into iron(0) nanoparticles according to eq 1^{60,61}



where n is the amount of hydroxyl groups oxidized by Fe³⁺, and Ar is a phenyl group contained in palm waste extract. The FTIR analysis revealed the presence of phenolic compounds in the HB-NZVI sample.

Then, 1.0 mol/L NaOH solution was gradually added until the pH of 6.0 was attained, which conferred the high yield of NZVI.⁶² The obtained solid was separated from solution by centrifugation at 3500 rpm for 5 min and washed several times with distilled water to remove the excess of Fe³⁺ and the

extract. Finally, the HB-NZVI nanoparticles were dried overnight in an oven at 60 and then ground to fine powder.⁵⁹

2.2.2. Characterization Techniques. The surface structure and morphology of HB and HB-NZVI were examined by scanning electron microscopy (FEI Quanta 400 FEG, Hillsboro, OR, USA) and TEM (JEOL-2100F, Japan). Their chemical properties were highlighted by a Fourier-transform infrared spectrometer (Nicolet Instruments, Nexus 870, Madison, WI, USA). The FTIR spectra were carried out in the range of 400–4000 cm⁻¹. The HB-NZVI size distribution and zeta potential values were obtained by dynamic laser scattering (DLS) analysis using typical cuvettes. The size and morphology were assessed by transmission electron microscopy analysis (JEM-3100F JEOL 3010 instrument with a UHR pole piece). The BET surface areas were evaluated using a Quanta Chrome Nova 3000e automated surface area analyzer (American Quanta Chrome Instruments Company, USA). To study the stability of HB-NZVI as a catalyst, the XRD spectrum of HB-NZVI before and after use was recorded using an X-ray diffractometer (PXRD-6000 SHIMADZU) with a

voltage of 40 kV and a current of 30 mA with Cu K α radiation ($K = 1.54056 \text{ \AA}$) in the angle range of 10–80 °C.

2.2.3. Tests of COG Oxidation. The COG degradation experiments were carried out in batch mode under magnetic stirring under different conditions. HB-NZVI was first weighed (10 to 70 mg) and added to an Erlenmeyer flask containing 100 mL of COG solution (initial concentration of 10–40 mg) at adjusted initial pH (2 to 7) by adding diluted solutions of sulfuric or sodium hydroxide solutions. Subsequently, H₂O₂ (3–7 10^{-5} mol) was added to the suspension that was continuously stirred for 3 h at fixed temperature (20 to 50 °C).

At the predetermined interval time, 1.5 mL of the reaction suspension was sampled and filtered through a 0.45 μm PES syringe filter. Subsequently, approximately 1 mL of the filtered solution was analyzed using a UV–visible spectrophotometer (PG Instruments-TI 80) at 495 nm to determine the residual COG concentration.

The removal efficiency of COG (R) was calculated using the following equation:

$$R = \frac{C_0 - C_t}{C_0} \times 100\% \quad (2)$$

where C_0 is the initial COG concentration in the solution (mg/L), and C_t is the COG concentration at time t (mg/L).

2.2.4. Chemical Oxygen Demand (COD) Removal. COG degradation was also tested by COD removal using a titrimetric method with K₂Cr₂O₇ as an oxidant at acidic pH and Ag₂SO₄ as a catalyst at 165 °C for 2 h.⁶³ The following equation was used to compute the percentage of COD removal:

$$\text{COD} = \frac{\text{COD}_0 - \text{COD}_f}{\text{COD}_0} \times 100\% \quad (3)$$

where COD_0 is the initial COD value, and COD_f is COD after reaction.

It should be noted that all experiments were performed in duplicate or triplicate, and the results shown are means with a relative error of 3%.

3. RESULTS AND DISCUSSION

3.1. Characterization of HB-NZVI and HB. **3.1.1. SEM Analysis.** The SEM analysis result (Figure 1a) revealed that the nanoparticles of NZVI were mostly spherical and formed prominent chain-like aggregates. This aggregation decreased the reaction activity of NZVI nanoparticles and could be ascribed to the magnetic attraction with NZVI nanoparticles. As shown in the SEM image of HB-NZVI (Figure 1b), the aggregation of NZVI nanoparticles significantly decreased after nanoparticles were loaded to HB, which became coarse than HB (Figure 1c). Therefore, HB can be used for better NZVI nanoparticle dispersion.

3.1.2. Zeta Potential and DLS Analysis. The zeta potential, hydrodynamic diameter, and polydispersity index (PDI) values were measured at 25 °C by dynamic light scattering (DLS). Negative zeta values of –27.8 and –20.6 were found for HB and HB-NZVI, respectively (Table 3), indicating the poor degree of agglomeration to both materials. Indeed, a value between –30 and 30 mV is associated with good nanoparticle stability.^{64,65} We can conclude that they are stable in the conditions in which they are to be used. Particle sizing is an important characterization technique to confirm the production of nano-sized particles. The particle size of the HB-NZVI

Table 3. Dynamic Light Scattering Analysis of HB-NZVI and Clay HB

	z-average size (nm)	PDI	PDI width (nm)
HB clay	58	0.8	5.172
HB-NZVI	91	1	9.119

nanoparticles and bentonite clay HB is the hydrodynamic diameter (intensity weighted mean diameter or the z-average diameter) of the particle size distribution. Based on results of DLS analysis depicted in Table 3, the HB-NZVI nanoparticles have a mean diameter of 91 nm and those of HB have the size of 58 nm. The PDI values of HB-NZVI and clay HB are 1 and 0.8, respectively, which is less than 1, suggesting a monodisperse particulate system⁶⁶ with a PDI width between 5 and 10 nm.

3.1.3. TEM Analysis. The chain-like and/or fiber-like iron structures, shown in the NZVI TEM images (Figure 2a), are similar to those found in the high-magnification SEM image (Figure 1a). Compared to TEM images of NZVI, TEM images of HB-supported NZVI nanoparticles (Figure 2b) reveal marked differences. Irregular rectangular-shaped nanoparticles were formed, probably due to the existence of polyphenols on the surface of the nanoparticles.⁸¹ However, other studies have shown that the iron nanoparticles are produced as irregular spherical particles.⁸² This dependence on the percentage of polyphenols present in the extract can cause different reactions and hinder or promote the growth of NZVI nanoparticles, thus producing different sizes and shapes of iron nanoparticles.⁸³ Therefore, HB can be used for better dispersion of NZVI nanoparticles. Figure 2 displays various magnifications of TEM images of NZVI (a) and HB-NZVI (b) and demonstrates that there is no aggregation of charged NZVI on bentonite clay. The average size of the nanoparticles is calculated from the MS data using Image J.51j8 software. As shown in Figure 2c, the particle size distribution of HB-NZVI had an average diameter of approximately 45 nm. Thus, NZVI was successfully loaded onto the surface or embedded in the bentonite nanosheets. It can be noted that the hydrodynamic size of NZVI measured by DLS (Table 3) was larger than the size measured by TEM.

3.1.4. FTIR Spectroscopy Analysis. Figure 3 shows the FTIR spectra for the waste palm, NZVI, and HB-NZVI. The FTIR spectra of the synthesized NZVI and HB-NZVI show broadband stretching vibrations at 3292 and 3363 cm^{-1} for O–H, respectively, and indicate the presence of polyphenols.⁶⁷ The adsorption bands at 1500 and 1550 cm^{-1} for HB-NZVI and 1595 and 1516 cm^{-1} for NZVI correspond to the stretching vibrations of carbonyl groups and the deformation vibration of the C–C bonds in the phenolic groups absorbed in the 1500–1600 cm^{-1} region,⁶⁸ while the peak of NZVI at 1709 cm^{-1} is ascribed to C–O–C stretching vibration.⁶⁹ In addition, the weak absorption bands at 795 and 528 cm^{-1} are attributed to Fe–O stretching vibration of Fe oxide,^{70,71} which confirm properly the synthesis of NZVI particles. After NZVI is loaded on the surface of bentonite, it is observed that several peaks disappear or shift because of the interaction of the functional groups existing on HB and NZVI. These changes prove the successful loading and immobilization of NZVI particles on bentonite fibers. The O–H stretching vibrations of Al–OH, Al, and adsorbed H₂O molecules and O–H bending vibration of the adsorbed water molecule were observed at 3620 and 3695 cm^{-1} and 3392 and 1632 cm^{-1} .^{70,72} The peak at 1427 cm^{-1} relates to the C–O stretching vibration of

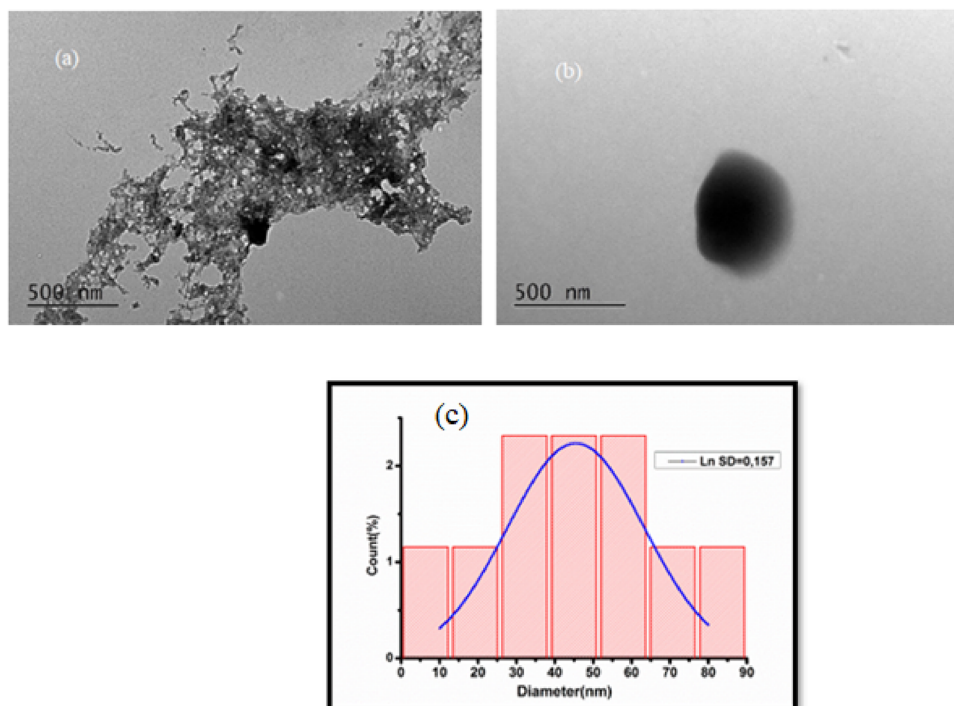


Figure 2. TEM images of NZVI (a) and HB-NZVI (b) and histogram of the diameter of HB-NZVI nanoparticle distribution (c).

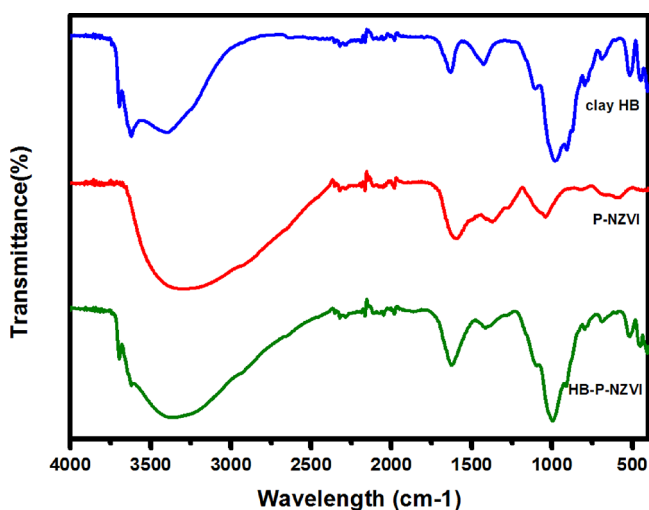


Figure 3. FTIR spectra of HB, NZVI, and HB-NZVI samples.

carbonate impurity.⁷³ The peaks at 1166 and 980 cm^{-1} are assigned to the Si–O stretching vibration of bentonite tetrahedral sheets.⁴⁷ Also, the peaks at 447 and 406 cm^{-1} are assigned to the Si–O–Si bending vibration.⁷⁴

3.1.5. BET Surface Area Analysis. The BET specific surface area of synthesized nanomaterial (53.66 m^2/g) is significantly higher than that of the natural clay (26.18 m^2/g) (Table 4). This suggests that the presence of zero-valent nanoparticles significantly increases the surface area, which is critical in high-

Table 4. BET of HB-NZVI and Clay HB

	BET surface area (m^2/g)	pore volume (cm^3/g)	pore size (\AA)
HB clay	26.18	0.005	8.116
HB-P-NZVI	53.66	0.059	44.42

performance catalysts as the surface area of a porous material is one of the most useful microstructural parameters for defining its properties.^{75,76} As indicated in Table 4, the total pore volume of the produced nanomaterial increasing in comparison to the clay attests to the presence of mesopores created by the intercalated Fe nanoparticles.^{77,78} These findings are in good correlation with examinations conducted on similar materials.⁷⁹

3.2. Catalytic and Adsorptive Activities. To study the catalytic and adsorptive activities of HB, NZVI, and NZVI-HB, preliminary experiments were carried out to evaluate the oxidation by H_2O_2 and the adsorption of COG using 0.03 g of HB, 0.03 g of NZVI-HB, 0.03 g of NZVI, and 4×10^{-5} mol of H_2O_2 , which were introduced into the solution of COG (100 mL, 20 mg/L at pH 3) and magnetically stirred at room temperature. After 180 min of reaction, the suspensions were filtered through 0.45 μm membranes and filtrates were analyzed by spectrophotometry to determine the residual concentration of COG. Figure 4 shows the COG dye removal

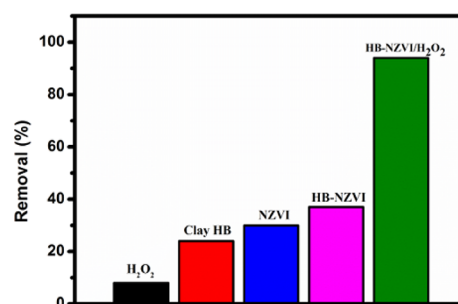


Figure 4. COG removal efficiency under different conditions (catalyst mass (HB-NZVI) = 0.3 g/L, catalyst mass (NZVI) = 0.3 g/L, mass (clay HB) = 0.3 g/L, $[\text{H}_2\text{O}_2]$ = 4×10^{-4} mol/L, $[\text{COG}]$ = 20 mg/L, room temperature, pH 3, 3 h).

Scheme 1. Plausible Mechanism for the Removal of COG onto HB-NZVI

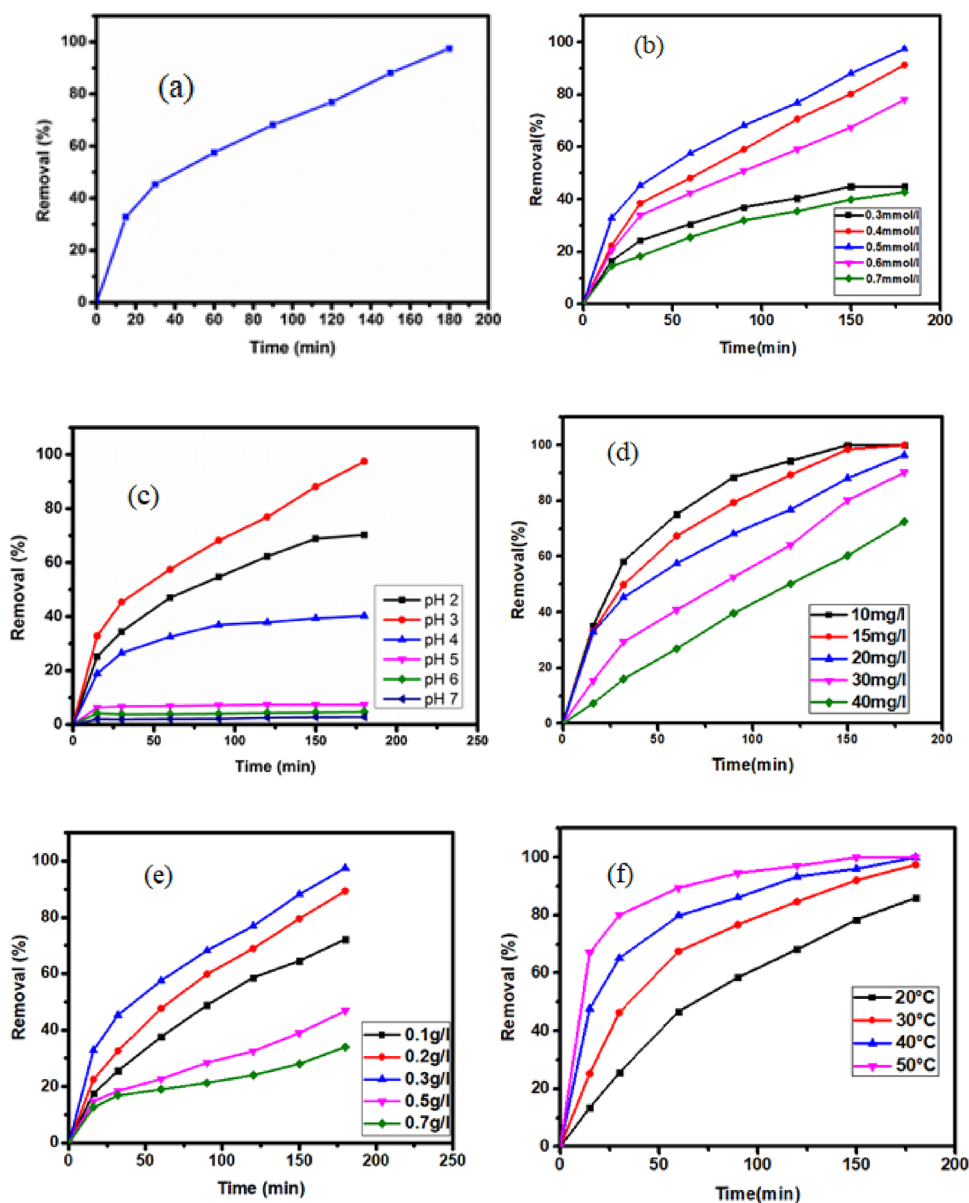
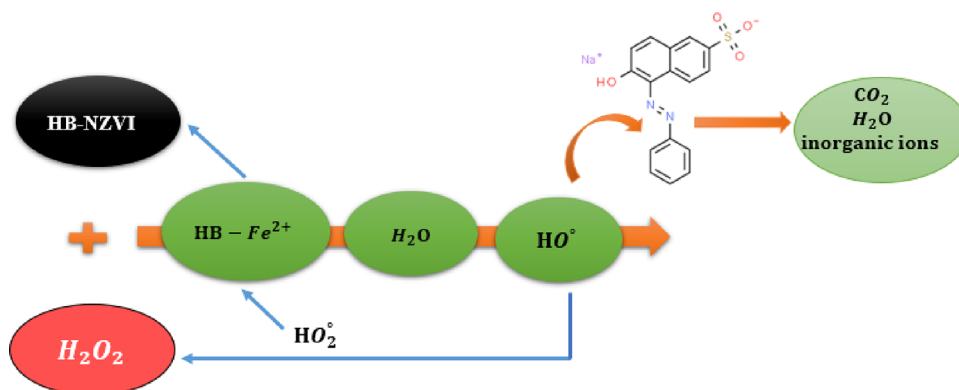
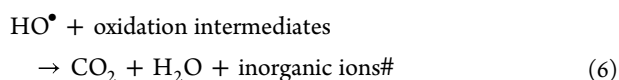
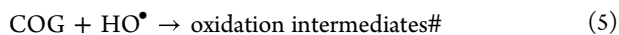
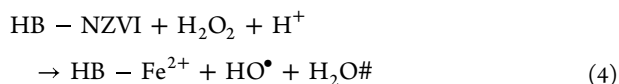


Figure 5. (a) Effect of contact time on degradation COG, (b) effect of H₂O₂ concentration on the removal of COG, (c) effect of pH on the removal of COG, (d) effect of the initial concentration of COG on the removal of COG, (e) effect of catalyst mass on the removal of COG, and (f) effect of temperature on the removal of COG.

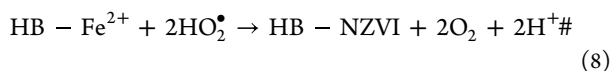
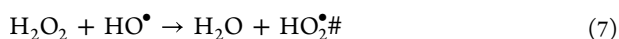
efficiency in the five cases. When only H₂O₂ was added to COG solution, only 8% of dye was degraded, indicating that

without a catalyst, H₂O₂ cannot effectively degrade COG. The removal efficiencies of COG by HB and NZVI were 24 and

30%, respectively, indicating lower COG removal. HB-NZVI could only adsorb 37% of COG. Indeed, 98% degradation of COG is achieved when adsorption is coupled with the Fenton-like reaction, which involves interactions of COG, HB-NZVI, and H₂O₂ (to be studied below). The degradation mechanisms of COG in the Fenton-like reaction system could be proposed as follows. H₂O₂ reacts with fixed active sites on the HB-NZVI surface to give hydroxyl radicals (HO•), which ensure the COG degradation and mineralization:



HB-NZVI regeneration may occur according to these reactions:



In summary, the mechanism of COG removal by HB-NZVI involves both the adsorption of COG by HB-NZVI and its degradation via a Fenton-like reaction as proposed in Scheme 1.

3.3. Parametric Study of COG Catalytic Oxidation Using HB-NZVI.

3.3.1. Effect of Reaction Time on COG Degradation. The effect of reaction time on COG degradation by HB-NZVI is shown in Figure 5a. The rate of COG degradation was 55% in the first 0.5 h and reached 98% at 3 h. Subsequently, the COG degradation rate of 100% was observed after 5 h.

3.3.2. Effect of H₂O₂ Concentration on COG Degradation. The concentration of hydrogen peroxide is a very important parameter for the maximum degradation efficiency of COG dye from aqueous solutions. The concentration of HB-NZVI was fixed at 0.3 g/L. Afterward, the effect of different concentrations of H₂O₂ on the removal of aqueous dye solution (20 mg/L) at an initial pH of 3 and at room temperature was investigated. Figure 5b illustrates the influence of H₂O₂ concentration and oxidative reaction time on the degradation of COG dye solution. The degradation efficiency increased with a rise in hydrogen peroxide concentration from 0.4 to 0.6 mmol/L. This was indeed caused by the high production of hydroxyl free radicals (•OH) when the amount of H₂O₂ was increased. Further, an increase in H₂O₂ by over 0.5 mmol/L led to decreased removal efficiency. In fact, when the H₂O₂ concentration was increased from 0.5 to 0.7 mmol/L, the degradation efficiency decreased from 100 to 42.8%. The recombination of hydroxyl radicals or the reaction of OH• with an excess of H₂O₂ may be responsible for this behavior.⁸⁰ As a result, •OH radicals were consumed.^{81,82} Therefore, the hydrogen peroxide concentration of 0.5 mmol/L was chosen as the optimum concentration and was used in the following set of experiments.

3.3.3. Effect of pH on COG Degradation. The influence of pH was examined in the 3–11 range using solutions containing 30 mg/L COG and 0.3 g/L HB-NZVI at room temperature.

Figure 5c shows that pH significantly influenced COG degradation as it controls the catalytic activity, oxidant and substrate activities, dominant Fe species, and stability. HB-NZVI showed high COG degradation efficiency at pH 3. When the pH value of the solution increases from 3.0 to 7.0, the degradation efficiency of COG decreases from 100 to 5% within 3 h of reaction, but any reaction was observed at pH 9 and 11. Likewise, when the pH value decreased from 3.0 to 2.0, the degradation efficiency of dye declines from 100 to 72%. Above pH 5, COG degradation is low, which can be explained by the electrostatic repulsion between negatively charged HB-NZVI (pH_{zpc} 4.7) and COG in H L⁻ form. For pH > 3.0, the oxidation potential of HO• decreases, resulting in the lower degradation efficiency of COG. In fact, the oxidation potential of the redox couple HO•/H₂O is 2.59 V at pH 0 and that of HO•/OH⁻ is 1.64 V at pH 14.^{83,84} On the other hand, in lower pH conditions (pH < 3.0), hydrogen peroxide formed a stable oxonium ion H₃O₂⁺⁸⁵ (reaction 9), which considerably reduces its decomposition into hydroxyl radicals. Moreover, the scavenging of HO• by H⁺ is enhanced in this pH range. Consequently, the degradation efficiency of COG decreased.



Therefore, the optimum pH value was equal to 3.0.

3.3.4. Effect of the Initial Concentration of COG. Figure 5d shows the influence of the initial concentration of dye on the decolorization of COG dye. The experimental conditions are as follows: [H₂O₂] = 5 × 10⁻⁴ mol/L, catalyst dose = 0.3 mg/L, t = 180 min, pH = 3, room temperature. When the initial COG dye concentration increased from 10 to 40 mg/L for HB-NZVI, the decolorization efficiency decreased from 100 to 72.6%. As shown in Figure 6d, the COG degradation efficiency depends strongly on its initial concentration. The higher the initial concentration of dye, the greater the time required for its degradation. For example, the percentage removal attained after 120 min was 100% for an initial concentration of 10 mg/L and only less than 60% for an initial concentration equal to 40 mg/L. This behavior could be because the number of dye molecules is increased, but the number of HO• remains constant. On the other hand, as the initial concentration of the pollutant increases, more molecules of solute can be adsorbed on the surface of the catalyst.⁸⁶ Consequently, the generation of HO• radicals would be reduced since pollutant molecules occupy the active sites.

3.3.5. Effect of the Amount Catalyst on COG Degradation. The amount of utilized catalyst influenced the degradation tendency of COG by HB-NZVI, as illustrated in Figure 5e. An increase in the amount of HB-NZVI ranging from 0.1 g to 0.3 g/L increased the degradation ratio from 72 to 100%, which resulted from the formation of additional active sites on the surface of the catalyst, as well as an increased generation rate of free O•H.^{87,88} This result clearly indicated that the degradation of COG by HB-NZVI was due to the amount of O•H generated on the NZVI particle surfaces.^{89,90} Figure 5e shows that the increase for HB-NZVI from 0.3 to 0.7 g/L resulted in the decrease in degradation ratio from 100 to 34% due to the self-destruction of HO•. Consequently, the optimum catalyst dosage for HB-NZVI was 0.3 g/L.

3.3.6. Effect of Temperature. The effect of temperature on the removal of COG was investigated by varying the temperature value from 20 to 50 °C while keeping constant the initial COG concentration, initial pH, H₂O₂ concentration, time reaction, and HB-NZVI catalyst loading at 20 mg/L, 3, 5

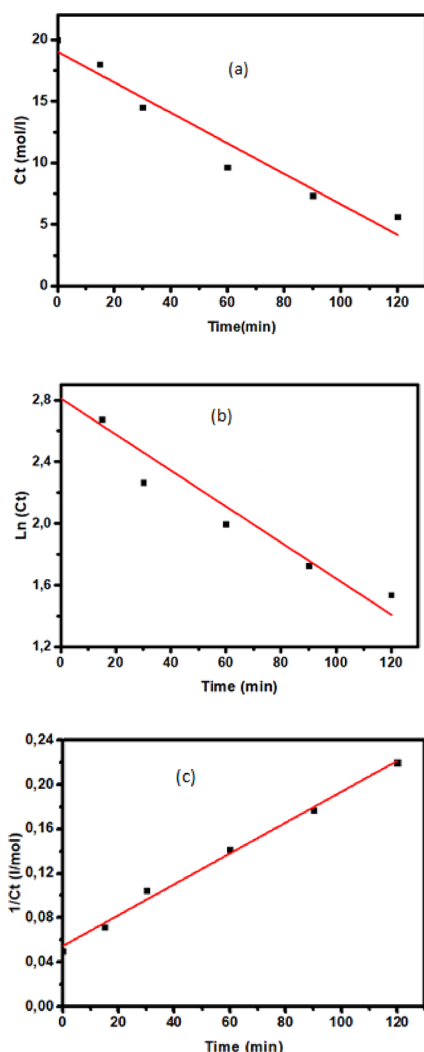


Figure 6. Linear plots of kinetic data calculated by the pseudo-zero-order (a), pseudo-first-order (b), and pseudo-second-order (c) models ($[\text{COG}] = 20 \text{ mg/L}$, $[\text{H}_2\text{O}_2] = 5 \times 10^{-4} \text{ mol/L}$, catalyst dose = 0.20 mg/L , $\text{pH} = 3$, $t = 120 \text{ min}$, $T = 30 \text{ }^\circ\text{C}$).

$\times 10^{-4} \text{ mol/L}$, 180 min , and 0.20 g/L , respectively. Higher temperatures than $50 \text{ }^\circ\text{C}$ are not recommended because they will cause significant evaporation of the solution during the experiments, decrease the solubility of oxygen in water, and induce the self-decomposition of hydrogen peroxide, which are not desirable.⁹¹ As shown in Figure 5f, the degradation of COG dye was positively impacted by the rise in temperature. When the temperature was raised from 20 to $50 \text{ }^\circ\text{C}$ after 3 h of HB-NZVI-catalyzed processes, the degradation efficiency increased from 77 to 100% . This may be explained by the fact that higher temperatures have a tendency to speed up the oxidation process between the catalyst and H_2O_2 , increasing the rate at which hydroxyl free radicals (O^\bulletH) or high-valence iron species were produced.^{92,93}

3.3.7. Kinetic Study and Activated Energy. The degradation of COG and its intermediate products is carried out by the $\cdot\text{OH}$ generated by the system (reactions 4 and 5), and then the rate equation of the reaction can be expressed as:

$$-\frac{dC}{dt} = k \times C_1^p \times C_2^n \quad (10)$$

Thus, by assuming that the hydroxyl radical concentration was a constant, eq 10 may be simplified to:⁹⁴

$$-\frac{dC}{dt} = k_{\text{app}} \times C_2^n \quad (11)$$

where C_1 is the concentration of $\cdot\text{OH}$ in solution, C_2 is the concentration of COG in solution, K is the reaction rate constant, p and n are reaction orders, t is the reaction time, and k and k_{app} are the apparent and pseudo-reaction order, respectively.

To describe quantitatively the effect of the applied temperature on the reaction kinetics, the pseudo-zero-order, pseudo-first-order, and pseudo-second-order models were applied to data of Figure 5f according to eqs 12–14, and the obtained results are depicted in Figure 6.

$$C_t = C_0 - k_0 t \quad (12)$$

$$\ln \frac{C_0}{C_t} = k_1 t \quad (13)$$

$$\frac{1}{C_t} - \frac{1}{C_0} = k_2 t \quad (14)$$

where k_0 , k_1 , and k_2 are the rate constants for pseudo-zero-, pseudo-first-, and pseudo-second-order reactions, respectively. Figure 6 shows the linear plots of kinetic data calculated by the pseudo-zero-order (a), pseudo-first-order (b), and pseudo-second-order (c) models.

As shown in Table 5, the experimental data were better fitted by the pseudo-second-order model since the correlation

Table 5. Correlation Coefficients R^2 of the Pseudo-Zero-, Pseudo-First-, and Pseudo-Second-Order Kinetic Models

	kinetic model		
	zero	first	second
R^2	0.9548	0.9431	0.9947
C_0 (mg/L)	18.212	22.354	19.784

coefficient R^2 is higher than those of pseudo-zero- and pseudo-first-order models. In addition, the calculated value of C_0 in the case of the pseudo-second-order model is practically equal to the experimental value of 20 mg/L .

The values of rate constant obtained at different temperatures were used to calculate the energy of activation by using the Arrhenius equation (eq 15):⁹⁵

$$\ln K = \frac{-E_a}{RT} + \ln A_0 \quad (15)$$

where E_a (J/mol) is the apparent activation energy, and A_0 is the pre-exponential factor with the same dimension as k . R is the gas constant ($8.314 \text{ J}\cdot\text{K}^{-1}\cdot\text{mol}^{-1}$), and T is the temperature in K. Activation energy (E_a) and factor (A_0) can be calculated through the slope and intercept of this linear regression equation, respectively. The curve of variation of the Arrhenius plot of $\ln k$ versus $1/T$ (not shown) exhibited a good linear relationship ($R^2 = 0.9988$). From the slope of the line, E_a was computed. The E_a of ordinary thermal reactions is usually between 60 and $250 \text{ kJ}\cdot\text{mol}^{-1}$ in general,^{96,97} so the E_a value of $33.1 \text{ kJ}\cdot\text{mol}^{-1}$ indicated that the oxidation of COG by the heterogeneous Fenton-like reaction proceeded with a low energy barrier and can easily be activated. Moreover, an activation energy of 33.11 kJ/mol was reported for the rapid

decolorization of azo dye methyl orange in aqueous solution by nanoscale zero-valent iron particles. Likewise, the literature reported that the homogeneous catalytic Fenton oxidation of azo dye had an activation energy of 25.21 kJ/mol.⁹⁸ The activation energy obtained in this study for the COG oxidation is very close to that given for the latter azo dye oxidation. The degradation of COG dye using HB-NZVI was calculated to be 33.11 kJ/mol. This type of adsorption is considered physical adsorption that requires a low activation energy amount of 5–40 kJ/mol,⁹⁹ thus confirming the physically diffusion-controlled reaction in the degradation of COG dye using HB-NZVI.

3.4. COD Removal. The mineralization efficiency of COG was further studied by measuring COD removal rate under previously established optimal conditions: $[\text{H}_2\text{O}_2] = 5 \times 10^{-4}$ mol/L, $[\text{COG}] = 20$ mg/L, dose catalyst = 0.2 g/L, pH = 3, $t = 180$ min, room temperature or 30 °C. It is widely known that the total discoloration of organic dyes does not necessarily indicate that they have completely mineralized into carbon dioxide and water.¹⁰⁰ Indeed, during the discoloration of dyes, several colorless intermediates with a COD value might be formed.¹⁰¹ Therefore, in addition to the discoloration, we focused on the COD removal of the COG solution after oxidation rather than the identification of reaction intermediates, which will be the subject of further studies. The COD is a measure of the oxygen needed to oxidize the organic matter present in the water, and it indirectly indicates the content of organic matter in the water.^{102–104} Under the optimum oxidation conditions, the percentage of COD removal by oxidation of COG was found to be 59% after 5 h of reaction. Other researchers have reported similar results and assigned the remained COD to organic intermediates.^{92,94,105,106}

3.5. Reusability and Stability of HB-NZVI. Reusability and stability are very important criteria for evaluating the practical application of catalysts. Successive cycles of the Fenton degradation were carried out to evaluate the stability and reusability of our catalyst under optimal conditions. After each successive cycle, HB-NZVI was separated by centrifugation after the COG dye had completely oxidized. It was then cleaned with distilled water several times, dried in an air oven for 12 h at 60 °C, and tested for the subsequent oxidation run. As shown in Figure 7, the catalyst could be successfully reused for four successive degradation cycles with more than 88% degradation efficiency, indicating that the HB-NZVI Fenton-like catalyst is stable.

Moreover, the stability of HB-NZVI before and after four times use was examined by XRD. As can be seen from Figure 8,

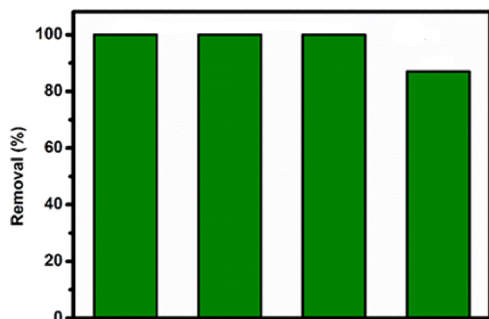


Figure 7. Reusability of HB-NZVI in COG dye removal.

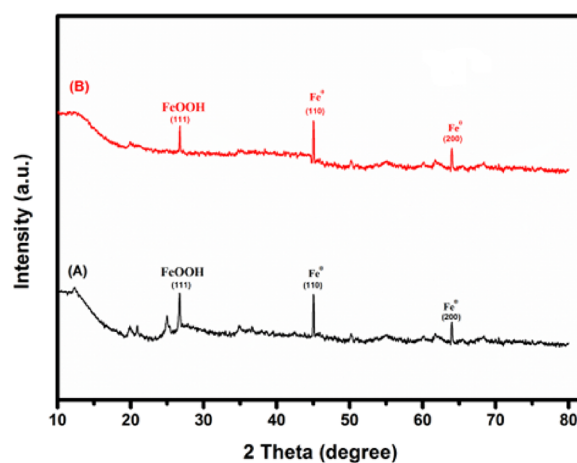


Figure 8. X-ray diffraction spectra of HB-NZVI: (A) before the reaction and (B) after the reaction.

the XRD patterns of HB-NZVI do not change before and after degradation. In both XRD patterns, the broad peak at 2θ value below 20.5° corresponds to characteristic peaks of bentonite clay.¹⁰⁷ The diffraction peaks with high intensities at $2\theta = 44.69^\circ$ and 62.87° corresponding to the (110) and (200) planes respectively indicate the presence of zero-valent iron.^{70,108} Meanwhile, the peak at $2\theta = 28.35^\circ$ corresponding to the (111) plane is attributed to iron hydroxides.^{109,110} Finally, the peaks at $2\theta = 8.49^\circ$, 20.83° , and 24.94° are associated with the organic matter on the surface of HB-NZVI,¹¹¹ in particular, polyphenol compounds.^{112,113} As shown in Figure 8B, the peaks of organic matter and polyphenols almost disappeared after COG oxidation. These experimental results reveal the stability of the catalyst structure after use.

3.6. Comparison of COG Removal Efficiency with Various Catalysts. The COG removal efficiency of the HB-NZVI composite prepared in this work is compared to other related catalysts reported in the literature, and the result is listed in Table 6. It is clear that the HB-NZVI composite displays excellent catalytic performance for COG dye under different conditions. Moreover, raw materials like waste palm and bentonite clay used in this work are cheap, easily available, safe, and non-toxic. The synthesis process of the HB-NZVI composite is also simple and can be used in large-scale production. Hence, the synthesized HB-NZVI composite can be employed as a suitable catalyst for the degradation of dye in aqueous solution.

4. CONCLUSIONS

NZVI-bentonite composite material was prepared via a reduction by palm waste extract. Various characterizations and analyses asserted the presence of NZVI particles into the surface of bentonite, which exhibited low aggregation and abundant reaction sites.

The effects of various experimental conditions such as reaction time, dosages of catalysts, concentration of H_2O_2 , temperature, and initial concentration of COG dye were investigated. The results show that the oxidative degradation efficiency of COG dye catalyzed by HB-NZVI was 100% under the optimum reaction conditions: $[\text{H}_2\text{O}_2] = 5 \times 10^{-4}$ mol/L, $[\text{COG}] = 20$ mg/L, dose catalyst = 0.2 g/L, pH = 3, $t = 180$ min, room temperature. Three kinetic models were applied, and the pseudo-second-order model was found the best model

Table 6. Comparison of COG Dye Removal under Different Oxidation Processes

COG (mg/L)	catalyst	removal efficiency (%)	reaction time (h)	oxidation process	reference
7	ZnO@Fe ₃ O ₄	80	0.5	peroxymonosulfate (PMS)	114
10	tungsten oxide nanopowder	87.5	3	photocatalytic degradation	115
100		97	0.33	sodium hypochlorite	116
500		99	0.66	electro-peroxone	117
20	HB-NZVI	100	3	heterogeneous Fenton-like	our work

representing the experimental kinetic data of COG dye degradation. The value of activation energy of 33.11 kJ/mol for HB-NZVI suggests a typical physically controlled reaction. Moreover, the HB-NZVI catalyst was found efficient after four cycles of use. This simple synthesis process of stable iron nanoparticles supported on clay via the waste palm will be beneficial to the large-scale production of highly effective catalysts. This work suggests that the HB-NZVI composite has great potential for remediation of dye wastewater.

A further study of HB-NZVI with the H₂O₂ Fenton-like reaction pathway and its intermediate products by high-performance liquid chromatography–mass spectrometry would be interesting to suggest. The scope of future work includes investigation of the degradation of emerging contaminants using HB-NZVI and changes in the active sites of the catalyst during the reaction and can show a possibility of coupling the process with photo-Fenton degradation of COG from aqueous solution using UV or visible light and HB-NZVI as the catalyst of H₂O₂. Additionally, future work will use real water samples from Tunisia textile factories.

AUTHOR INFORMATION

Corresponding Authors

Dhiss Tesnim – National School of Engineers of Gabes, Laboratory of Research: Processes, Energy, Environment & Electrical Systems PEESE (LR18ES34), University of Gabes, 6029 Gabes, Tunisia; Email: dhisstesnim@gmail.com

Jesus Simal-Gandara – Nutrition and Bromatology Group, Analytical Chemistry and Food Science Department, Faculty of Science, Universidade de Vigo, E32004 Ourense, Spain; orcid.org/0000-0001-9215-9737; Email: jsimal@uvigo.es

Author

Ben Amor Hedi – National School of Engineers of Gabes, Laboratory of Research: Processes, Energy, Environment & Electrical Systems PEESE (LR18ES34), University of Gabes, 6029 Gabes, Tunisia

Complete contact information is available at: <https://pubs.acs.org/10.1021/acsomega.3c01333>

Notes

The authors declare no competing financial interest.

REFERENCES

- (1) Al-Rubai, H. F.; Hassan, A. K.; Ali, A. J. A. Use of Zero-Valent Iron Nanotechnology to Remove Two Azo Dyes and Study Their Decomposition Kinetics. *Iraqi J. Sci. Technol.* **2023**, *12*, 76–84.
- (2) Eskicioglu, L. Beyond Postcolonialism: The Urban and Social Realist Turn in Indian and Nigerian Literatures. PhD Thesis, Carleton University, 2022.
- (3) Santhanarajan, A.-E.; Rhee, C.; Sul, W. J.; Yoo, K.; Seong, H. J.; Kim, H.-G.; Koh, S.-C. Transcriptomic Analysis of Degradative Pathways for Azo Dye Acid Blue 113 in *Sphingomonas Melonis* B-2

from the Dye Wastewater Treatment Process. *Microorganisms* **2022**, *10*, 438.

(4) Singh, A.; Pal, D. B.; Mohammad, A.; Alhazmi, A.; Haque, S.; Yoon, T.; Srivastava, N.; Gupta, V. K. Biological Remediation Technologies for Dyes and Heavy Metals in Wastewater Treatment: New Insight. *Bioresour. Technol.* **2022**, *343*, No. 126154.

(5) Mathur, A.; Dubey, S.; Prasad, R.; Singh, R. P. Mycelial and Secretome Proteomic Dynamics of *L. Squarrosulus* AF5 in Azo Dye Degradation. *J. Environ. Chem. Eng.* **2023**, *11*, No. 109374.

(6) Pinheiro, L. R. S.; Gradissimo, D. G.; Xavier, L. P.; Santos, A. V. Degradation of Azo Dyes: Bacterial Potential for Bioremediation. *Sustainability* **2022**, *14*, 1510.

(7) Yan, J.; Wang, P.; Wang, L.; Jin, Q.; Ali, A. S.; He, Y.; Wang, Y.; Sun, Y.; Li, A.; Adwy, W.; Ahmed, R. H.; Han, X. Bio-Decolorization of Synthetic Dyes by a Novel Endophytic Fungus *Penicillium Janthinellum* LM5 from Blueberry Pulp. *Biochem. Eng. J.* **2023**, *195*, No. 108909.

(8) Hashemi, S. H.; Kaykhai, M. Azo Dyes: Sources, Occurrence, Toxicity, Sampling, Analysis, and Their Removal Methods. In *Emerging freshwater pollutants*; Elsevier, 2022; pp. 267–287, DOI: [10.1016/B978-0-12-822850-0.00013-2](https://doi.org/10.1016/B978-0-12-822850-0.00013-2).

(9) Zaheer, Z.; Bawazir, W. A.; Al-Bukhari, S. M.; Basaleh, A. S. Adsorption, Equilibrium Isotherm, and Thermodynamic Studies to the Removal of Acid Orange 7. *Mater. Chem. Phys.* **2019**, *232*, 109–120.

(10) Matome, S. M.; Makhado, E.; Katata-Seru, L. M.; Maponya, T. C.; Modibane, K. D.; Hato, M. J.; Bahadur, I. Green Synthesis of Polypyrrole/Nanoscale Zero Valent Iron Nanocomposite and Use as an Adsorbent for Hexavalent Chromium from Aqueous Solution. *S. Afr. J. Chem. Eng.* **2020**, *34*, 1–10.

(11) Lee, B.; Yoon, S.; Lee, J. W.; Kim, Y.; Chang, J.; Yun, J.; Ro, J. C.; Lee, J.-S.; Lee, J. H. Statistical Characterization of the Morphologies of Nanoparticles through Machine Learning Based Electron Microscopy Image Analysis. *ACS Nano* **2020**, *14*, 17125–17133.

(12) Kalderis, D.; Kayan, B.; Akay, S.; Kulaksız, E.; Gözmen, B. Adsorption of 2, 4-Dichlorophenol on Paper Sludge/Wheat Husk Biochar: Process Optimization and Comparison with Biochars Prepared from Wood Chips, Sewage Sludge and Hog Fuel/Demolition Waste. *J. Environ. Chem. Eng.* **2017**, *5*, 2222–2231.

(13) Song, M.; Hu, X.; Gu, T.; Zhang, W.; Deng, Z. Nanocelluloses Affixed Nanoscale Zero-Valent Iron (NZVI) for Nickel Removal: Synthesis, Characterization and Mechanisms. *J. Environ. Chem. Eng.* **2022**, *10*, No. 107466.

(14) Xiao, W.-D.; Xiao, L.-P.; Lv, Y.-H.; Yin, W.-Z.; Sánchez, J.; Zhai, S.-R.; An, Q.-D.; Sun, R.-C. Lignin-Derived Carbon Coated Nanoscale Zero-Valent Iron as a Novel Bifunctional Material for Efficient Removal of Cr (VI) and Organic Pollutants. *Sep. Purif. Technol.* **2022**, *299*, No. 121689.

(15) Keerthana, S. P.; Gayathri, S.; Yuvakkumar, R.; Kungumadevi, L.; Ravi, G.; Al-Sehemi, A. G.; Velauthapillai, D. Conversion and Reducing Agent Effect on Zero Valent Iron into Fe₃O₄ for Photocatalytic Degradation under UV Light Irradiation. *Environ. Res.* **2022**, *214*, No. 113959.

(16) Guo, B.; Xu, T.; Zhang, L.; Li, S. A Heterogeneous Fenton-like System with Green Iron Nanoparticles for the Removal of Bisphenol A: Performance, Kinetics and Transformation Mechanism. *J. Environ. Manage.* **2020**, *272*, No. 111047.

(17) Liu, X.; Wang, F.; Chen, Z.; Megharaj, M.; Naidu, R. Heterogeneous Fenton Oxidation of Direct Black G in Dye Effluent

Using Functional Kaolin-Supported Nanoscale Zero Iron. *Environ. Sci. Pollut. Res.* **2014**, *21*, 1936–1943.

(18) Hassani, A.; Eghbali, P.; Kakavandi, B.; Lin, K.-Y. A.; Ghanbari, F. Acetaminophen Removal from Aqueous Solutions through Peroxymonosulfate Activation by CoFe₂O₄/Mpg-C₃N₄ Nanocomposite: Insight into the Performance and Degradation Kinetics. *Environ. Technol. Innovation* **2020**, *20*, No. 101127.

(19) Pourshirband, N.; Nezamzadeh-Ejehieh, A. An Efficient Z-Scheme CdS/g-C₃N₄ Nano Catalyst in Methyl Orange Photo-degradation: Focus on the Scavenging Agent and Mechanism. *J. Mol. Liq.* **2021**, *335*, No. 116543.

(20) Zhang, M.; Dong, H.; Zhao, L.; Wang, D.; Meng, D. A Review on Fenton Process for Organic Wastewater Treatment Based on Optimization Perspective. *Sci. Total Environ.* **2019**, *670*, 110–121.

(21) Ribeiro, J. P.; Nunes, M. I. Recent Trends and Developments in Fenton Processes for Industrial Wastewater Treatment—A Critical Review. *Environ. Res.* **2021**, *197*, No. 110957.

(22) Wang, Z.; Liu, M.; Xiao, F.; Postole, G.; Zhao, H.; Zhao, G. Recent Advances and Trends of Heterogeneous Electro-Fenton Process for Wastewater Treatment-Review. *Chin. Chem. Lett.* **2022**, *33*, 653–662.

(23) Hussain, S.; Aneggi, E.; Goi, D. Catalytic Activity of Metals in Heterogeneous Fenton-like Oxidation of Wastewater Contaminants: A Review. *Environ. Chem. Lett.* **2021**, *19*, 2405–2424.

(24) Sampaio, E. F. S.; Guimarães, V.; Soares, O. S. G. P.; Pereira, M. F. R.; Rodrigues, C. S. D.; Madeira, L. M. Degradation of Toluene from Gas Streams by Heterogeneous Fenton's Oxidation in a Slurry Bubble Reactor with Activated Carbon-Based Catalysts. *Nanomaterials*, *12* (), 3274, DOI: 10.3390/nano12193274.

(25) Pachamuthu, M. P.; Karthikeyan, S.; Maheswari, R.; Lee, A. F.; Ramanathan, A. Fenton-like Degradation of Bisphenol A Catalyzed by Mesoporous Cu/TUD-1. *Appl. Surf. Sci.* **2017**, *393*, 67–73.

(26) Xu, L.; Wang, J. A Heterogeneous Fenton-like System with Nanoparticulate Zero-Valent Iron for Removal of 4-Chloro-3-Methyl Phenol. *J. Hazard. Mater.* **2011**, *186*, 256–264.

(27) Ma, H.; Yu, B.; Wang, Q.; Owens, G.; Chen, Z. Enhanced Removal of Pefloxacin from Aqueous Solution by Adsorption and Fenton-like Oxidation Using NH₂-MIL-88B. *J. Colloid Interface Sci.* **2021**, *583*, 279–287.

(28) Shukla, S.; Oturan, M. A. Dye Removal Using Electrochemistry and Semiconductor Oxide Nanotubes. *Environ. Chem. Lett.* **2015**, *13*, 157–172.

(29) Li, R.; Jin, X.; Megharaj, M.; Naidu, R.; Chen, Z. Heterogeneous Fenton Oxidation of 2, 4-Dichlorophenol Using Iron-Based Nanoparticles and Persulfate System. *Chem. Eng. J.* **2015**, *264*, 587–594.

(30) Wang, L.; Yang, J.; Li, Y.; Lv, J.; Zou, J. Removal of Chlorpheniramine in a Nanoscale Zero-Valent Iron Induced Heterogeneous Fenton System: Influencing Factors and Degradation Intermediates. *Chem. Eng. J.* **2016**, *284*, 1058–1067.

(31) Deng, J.; Dong, H.; Zhang, C.; Jiang, Z.; Cheng, Y.; Hou, K.; Zhang, L.; Fan, C. Nanoscale Zero-Valent Iron/Biochar Composite as an Activator for Fenton-like Removal of Sulfamethazine. *Sep. Purif. Technol.* **2018**, *202*, 130–137.

(32) Zha, S.; Cheng, Y.; Gao, Y.; Chen, Z.; Megharaj, M.; Naidu, R. Nanoscale Zero-Valent Iron as a Catalyst for Heterogeneous Fenton Oxidation of Amoxicillin. *Chem. Eng. J.* **2014**, *255*, 141–148.

(33) Tang, H.; Wang, J.; Zhang, S.; Pang, H.; Wang, X.; Chen, Z.; Li, M.; Song, G.; Qiu, M.; Yu, S. Recent Advances in Nanoscale Zero-Valent Iron-Based Materials: Characteristics, Environmental Remediation and Challenges. *J. Cleaner Prod.* **2021**, *319*, No. 128641.

(34) *Green synthesis and application of nanoscale zero-valent iron/rectorite composite material for P-chlorophenol degradation via heterogeneous Fenton reaction*; Elsevier Enhanced Reader. DOI: 10.1016/j.jscs.2019.02.001.

(35) Sun, Y.-P.; Li, X.; Cao, J.; Zhang, W.; Wang, H. P. Characterization of Zero-Valent Iron Nanoparticles. *Adv. Colloid Interface Sci.* **2006**, *120*, 47–56.

(36) Góral, D.; Marczuk, A.; Góral-Kowalczyk, M.; Koval, I.; Andrejko, D. Application of Iron Nanoparticle-Based Materials in the Food Industry. *Materials* **2023**, *16*, 780.

(37) Sfameni, S.; Rando, G.; Plutino, M. R. Sustainable Secondary-Raw Materials, Natural Substances and Eco-Friendly Nanomaterial-Based Approaches for Improved Surface Performances: An Overview of What They Are and How They Work. *Int. J. Mol. Sci.* **2023**, *24*, 5472.

(38) Raj, A.; Chowdhury, A.; Ali, S. W. Green Chemistry: Its Opportunities and Challenges in Colouration and Chemical Finishing of Textiles. *Sustainable Chem. Pharm.* **2022**, *27*, No. 100689.

(39) Hano, C.; Abbasi, B. H. Plant-Based Green Synthesis of Nanoparticles: Production, Characterization and Applications. *Biomolecules* **2022**, *12*, 31.

(40) Sharma, R.; Malaviya, P. Constructed Wetlands for Textile Wastewater Remediation: A Review on Concept, Pollutant Removal Mechanisms, and Integrated Technologies for Efficiency Enhancement. *Chemosphere* **2022**, *290*, No. 133358.

(41) Frost, R. L.; Xi, Y.; He, H. Synthesis, Characterization of Palygorskite Supported Zero-Valent Iron and Its Application for Methylene Blue Adsorption. *J. Colloid Interface Sci.* **2010**, *341*, 153–161.

(42) Xi, Y.; Megharaj, M.; Naidu, R. Dispersion of Zerovalent Iron Nanoparticles onto Bentonites and Use of These Catalysts for Orange II Decolourisation. *Appl. Clay Sci.* **2011**, *53*, 716–722.

(43) Ezzatahmedi, N.; Ayoko, G. A.; Millar, G. J.; Speight, R.; Yan, C.; Li, J.; Li, S.; Zhu, J.; Xi, Y. Clay-Supported Nanoscale Zero-Valent Iron Composite Materials for the Remediation of Contaminated Aqueous Solutions: A Review. *Chem. Eng. J.* **2017**, *312*, 336–350.

(44) Chen, Z.; Jin, X.; Chen, Z.; Megharaj, M.; Naidu, R. Removal of Methyl Orange from Aqueous Solution Using Bentonite-Supported Nanoscale Zero-Valent Iron. *J. Colloid Interface Sci.* **2011**, *363*, 601–607.

(45) Hür, C.; Erken, E. Assessment of Green Tea-Enabled Iron/Calcined Bentonite Nanocomposites for Phosphate Removal and Recovery. *J. Environ. Chem. Eng.* **2022**, *10*, No. 108519.

(46) Li, X.; Zhao, Y.; Xi, B.; Meng, X.; Gong, B.; Li, R.; Peng, X.; Liu, H. Decolorization of Methyl Orange by a New Clay-Supported Nanoscale Zero-Valent Iron: Synergetic Effect, Efficiency Optimization and Mechanism. *J. Environ. Sci.* **2017**, *52*, 8–17.

(47) Annan, E.; Nyankson, E.; Agyei-Tuffour, B.; Armah, S. K.; Nkrumah-Buandoh, G.; Hodasi, J. A. M.; Oteng-Peprah, M. Synthesis and Characterization of Modified Kaolin-Bentonite Composites for Enhanced Fluoride Removal from Drinking Water. *Adv. Mater. Sci. Eng.* **2021**, *2021*, 1.

(48) Li, Z.; Sun, Y.; Yang, Y.; Han, Y.; Wang, T.; Chen, J.; Tsang, D. C. W. Biochar-Supported Nanoscale Zero-Valent Iron as an Efficient Catalyst for Organic Degradation in Groundwater. *J. Hazard. Mater.* **2020**, *383*, No. 121240.

(49) Khalil, A. M. E.; Eljamal, O.; Amen, T. W. M.; Sugihara, Y.; Matsunaga, N. Optimized Nano-Scale Zero-Valent Iron Supported on Treated Activated Carbon for Enhanced Nitrate and Phosphate Removal from Water. *Chem. Eng. J.* **2017**, *309*, 349–365.

(50) Deng, Y.; Zhao, R. Advanced Oxidation Processes (AOPs) in Wastewater Treatment. *Curr. Pollut. Res.* **2015**, *1*, 167–176.

(51) Zhao, Q.; Zhao, X.; Cao, J. Advanced Nanomaterials for Degrading Persistent Organic Pollutants. In *Advanced Nanomaterials for Pollutant Sensing and Environmental Catalysis*; Elsevier, 2020; pp. 249–305, DOI: 10.1016/B978-0-12-814796-2.00007-1.

(52) Zayed, M. A.; Abdel-Gawad, S. A.; Abdel-Aziz, H. M.; Abo-Ayad, Z. A. Green Synthesis of Nano-Zero-Valent Copper for the D-Blue 60 Textile Dye Removal from Aqueous Medium. *Int. J. Environ. Res.* **2023**, *17*, 12.

(53) Pattanayak, D. S.; Pal, D.; Thakur, C.; Kumar, S.; Devnani, G. L. Bio-Synthesis of Iron Nanoparticles for Environmental Remediation: Status till Date. *Mater. Today: Proc.* **2021**, *44*, 3150–3155.

(54) Kangralkar, M. V.; Jayappa, M. Green Synthesis of Iron Nanoparticles by Terminalia Arjuna Bark Extract and Photo-degradation of Rose Bengal. *Iran. J. Catal.* **2020**, *10*, 181–188.

- (55) Wu, M.; Xu, X.; Lu, K.; Li, X. Effects of the Presence of Nanoscale Zero-Valent Iron on the Degradation of Polychlorinated Biphenyls and Total Organic Carbon by Sediment Microbial Fuel Cell. *Sci. Total Environ.* **2019**, *656*, 39–44.
- (56) Bourikas, K.; Styliadi, M.; Kondarides, D. I.; Verykios, X. E. Adsorption of Acid Orange 7 on the Surface of Titanium Dioxide. *Langmuir* **2005**, *21*, 9222–9230.
- (57) Tum, P. K. Nano-Photocatalytic Mineralization and Degradation of Dye Acid Orange 7 on Titanium Dioxide Coated Layers in a Batch Mode Plate Photo Reactor: Role of Flow Rate and Inorganic Salts. *Int. j. humanit. soc. sci.* **2022**, *10* (), DOI: 10.24940/thejhss/2022/v10/i4/HS2204-013.
- (58) Hamzeh, Y.; Ashori, A.; Azadeh, E.; Abdulkhani, A. Removal of Acid Orange 7 and Remazol Black 5 Reactive Dyes from Aqueous Solutions Using a Novel Biosorbent. *Mater. Sci. Eng., C* **2012**, *32*, 1394–1400.
- (59) Hassan, A. K.; Al-Kindi, G. Y.; Ghanim, D. Green Synthesis of Bentonite-Supported Iron Nanoparticles as a Heterogeneous Fenton-like Catalyst: Kinetics of Decolorization of Reactive Blue 238 Dye. *Water Sci. Eng.* **2020**, *13*, 286–298.
- (60) Mystrioti, C.; Sparis, D.; Papiasiopi, N.; Xenidis, A.; Dermatas, D.; Chrysochoou, M. Assessment of Polyphenol Coated Nano Zero Valent Iron for Hexavalent Chromium Removal from Contaminated Waters. *Bull. Environ. Contam. Toxicol.* **2015**, *94*, 302–307.
- (61) Deewan, R.; Yan, D. Y.-S.; Khamdahsag, P.; Tanboonchuy, V. Remediation of Arsenic-Contaminated Water by Green Zero-Valent Iron Nanoparticles. *Environ. Sci. Pollut. Res.* **2022**, 1–10.
- (62) Harshiny, M.; Iswarya, C. N.; Matheswaran, M. Biogenic Synthesis of Iron Nanoparticles Using Amaranthus Dubius Leaf Extract as a Reducing Agent. *Powder Technol.* **2015**, *286*, 744–749.
- (63) Rawat, S.; Singh, J. Fenton like Oxidative Degradation of Toxic Water Pollutants by Iron Nanoparticles Synthesized via Facile Green Route Using Waste Iron Rust as the Iron Precursor. *Environ. Eng. Res.* **2023**, *28*, 210621.
- (64) Vilardi, G.; Stoller, M.; Di Palma, L.; Boodhoo, K.; Verdona, N. Metallic Iron Nanoparticles Intensified Production by Spinning Disk Reactor: Optimization and Fluid Dynamics Modelling. *Chem. Eng. Process.* **2019**, *146*, No. 107683.
- (65) Zeta Potential - an overview; ScienceDirect Topics <https://www.sciencedirect.com/topics/earth-and-planetary-sciences/zeta-potential> (accessed 2022-11-15).
- (66) Araújo-Neto, R. P.; Silva-Freitas, E. L.; Carvalho, J. F.; Pontes, T. R. F.; Silva, K. L.; Damasceno, I. H. M.; Egito, E. S. T.; Dantas, A. L.; Morales, M. A.; Carriço, A. S. Monodisperse Sodium Oleate Coated Magnetite High Susceptibility Nanoparticles for Hyperthermia Applications. *J. Magn. Magn. Mater.* **2014**, *364*, 72–79.
- (67) Abdel-Aziz, H. M.; Farag, R. S.; Abdel-Gawad, S. A. Carbamazepine Removal from Aqueous Solution by Green Synthesis Zero-Valent Iron/Cu Nanoparticles with Ficus Benjaminia Leaves' Extract. *Int. J. Environ. Res.* **2019**, *13*, 843–852.
- (68) Ghitescu, R.-E.; Volf, I.; Carausu, C.; Bühlmann, A.-M.; Gilca, I. A.; Popa, V. I. Optimization of Ultrasound-Assisted Extraction of Polyphenols from Spruce Wood Bark. *Ultrason. Sonochem.* **2015**, *22*, 535–541.
- (69) Liu, J.; Mwamulima, T.; Wang, Y.; Fang, Y.; Song, S.; Peng, C. Removal of Pb (II) and Cr (VI) from Aqueous Solutions Using the Fly Ash-Based Adsorbent Material-Supported Zero-Valent Iron. *J. Mol. Liq.* **2017**, *243*, 205–211.
- (70) Sravanthi, K.; Ayodhya, D.; Swamy, P. Y. Green Synthesis, Characterization and Catalytic Activity of 4-Nitrophenol Reduction and Formation of Benzimidazoles Using Bentonite Supported Zero Valent Iron Nanoparticles. *Mater. Sci. Energy Technol.* **2019**, *2*, 298–307.
- (71) Mousavi, S. E.; Younesi, H.; Bahramifar, N.; Tamunaidu, P.; Karimi-Maleh, H. A Novel Route to the Synthesis of α -Fe₂O₃@ C@ SiO₂/TiO₂ Nanocomposite from the Metal-Organic Framework as a Photocatalyst for Water Treatment. *Chemosphere* **2022**, *297*, No. 133992.
- (72) Gandhi, D.; Bandyopadhyay, R.; Soni, B. Naturally Occurring Bentonite Clay: Structural Augmentation, Characterization and Application as Catalyst. *Mater. Today: Proc.* **2022**, *57*, 194–201.
- (73) Barakan, S.; Aghazadeh, V. Separation and Characterisation of Montmorillonite from a Low-Grade Natural Bentonite: Using a Non-Destructive Method. *Micro Nano Lett.* **2019**, *14*, 688–693.
- (74) Lingamdinne, L. P.; Koduru, J. R.; Chang, Y.-Y.; Kang, S.-H.; Yang, J.-K. Facile Synthesis of Flowered Mesoporous Graphene Oxide-Lanthanum Fluoride Nanocomposite for Adsorptive Removal of Arsenic. *J. Mol. Liq.* **2019**, *279*, 32–42.
- (75) Kerkez, D. V.; Tomašević, D. D.; Kozma, G.; Bečelić-Tomin, M. R.; Prica, M. D.; Rončević, S. D.; Kukovec, A.; Dalmacija, B. D.; Kónya, Z. Three Different Clay-Supported Nanoscale Zero-Valent Iron Materials for Industrial Azo Dye Degradation: A Comparative Study. *J. Taiwan Inst. Chem. Eng.* **2014**, *45*, 2451–2461.
- (76) Koutani, M.; Hayashi, E.; Kamata, K.; Hara, M. Synthesis and Aerobic Oxidation Catalysis of Mesoporous Todorokite-Type Manganese Oxide Nanoparticles by Crystallization of Precursors. *J. Am. Chem. Soc.* **2022**, *144*, 14090–14100.
- (77) Wu, M.; Teng, X.; Liang, X.; Zhang, Y.; Huang, Z.; Yin, Y. Supporting Nanoscale Zero-Valent Iron onto Shrimp Shell-Derived N-Doped Biochar to Boost Its Reactivity and Electron Utilization for Selenite Sequestration. *Chemosphere* **2023**, *319*, No. 137979.
- (78) Du, Y.; Fu, X.; Zhou, Q.; Zhao, J.; Wu, H.; Li, X.; Liu, Y.; Le, Z. Preparation of Zero-Valent Iron-Nickel Bimetallic Composite for Se (IV) Adsorption from Aqueous Solution. *J. Radioanal. Nucl. Chem.* **2023**, *332*, 785–796.
- (79) Baldermann, A.; Kaufhold, S.; Dohrmann, R.; Baldermann, C.; Letofsky-Papst, I.; Dietzel, M. A Novel NZVI–Bentonite Nanocomposite to Remove Trichloroethene (TCE) from Solution. *Chemosphere* **2021**, *282*, No. 131018.
- (80) Başkan, G. Removal of Antibiotics from Aqueous Solutions by Bentonite Supported-Nanoscale Zero-Valent Iron. *Int. J. Pioneering Technol. Eng.* **2022**, *1*, 46–56.
- (81) Hassan, A. K.; Rahman, M. M.; Chattopadhyay, G.; Naidu, R. Kinetic of the Degradation of Sulfanilic Acid Azochromotrop (SPADNS) by Fenton Process Coupled with Ultrasonic Irradiation or L-Cysteine Acceleration. *Environ. Technol. Innovation* **2019**, *15*, No. 100380.
- (82) Kuang, Y.; Wang, Q.; Chen, Z.; Megharaj, M.; Naidu, R. Heterogeneous Fenton-like Oxidation of Monochlorobenzene Using Green Synthesis of Iron Nanoparticles. *J. Colloid Interface Sci.* **2013**, *410*, 67–73.
- (83) O'Dowd, K.; Pillai, S. C. Photo-Fenton Disinfection at near Neutral PH: Process, Parameter Optimization and Recent Advances. *J. Environ. Chem. Eng.* **2020**, *8*, No. 104063.
- (84) Zhu, S.; Wang, W.; Xu, Y.; Zhu, Z.; Liu, Z.; Cui, F. Iron Sludge-Derived Magnetic Fe₀/Fe₃C Catalyst for Oxidation of Ciprofloxacin via Peroxymonosulfate Activation. *Chem. Eng. J.* **2019**, *365*, 99–110.
- (85) Bae, G.; Chung, M. W.; Ji, S. G.; Jaouen, F.; Choi, C. H. PH Effect on the H₂O₂-Induced Deactivation of Fe-NC Catalysts. *ACS Catal.* **2020**, *10*, 8485–8495.
- (86) Donkadokula, N. Y.; Kola, A. K.; Naz, I.; Saroj, D. A Review on Advanced Physico-Chemical and Biological Textile Dye Wastewater Treatment Techniques. *Rev. Environ. Sci. Biotechnol.* **2020**, *19*, 543–560.
- (87) Pullin, H.; Springell, R.; Parry, S.; Scott, T. The Effect of Aqueous Corrosion on the Structure and Reactivity of Zero-Valent Iron Nanoparticles. *Chem. Eng. J.* **2017**, *308*, 568–577.
- (88) Clarizia, L.; Russo, D.; Di Somma, I.; Marotta, R.; Andreozzi, R. Homogeneous Photo-Fenton Processes at near Neutral PH: A Review. *Appl. Catal., B* **2017**, *209*, 358–371.
- (89) Liu, X.; Zhou, Y.; Zhang, J.; Luo, L.; Yang, Y.; Huang, H.; Peng, H.; Tang, L.; Mu, Y. Insight into Electro-Fenton and Photo-Fenton for the Degradation of Antibiotics: Mechanism Study and Research Gaps. *Chem. Eng. J.* **2018**, *347*, 379–397.
- (90) Wang, N.; Zheng, T.; Zhang, G.; Wang, P. A Review on Fenton-like Processes for Organic Wastewater Treatment. *J. Environ. Chem. Eng.* **2016**, *4*, 762–787.

- (91) Pan, C.; Bian, G.; Zhang, Y.; Lou, Y.; Zhang, Y.; Dong, Y.; Xu, J.; Zhu, Y. Efficient and Stable H₂O₂ Production from H₂O and O₂ on BiPO₄ Photocatalyst. *Appl. Catal., B* **2022**, *316*, No. 121675.
- (92) Guo, X. X.; Hu, T. T.; Meng, B.; Sun, Y.; Han, Y.-F. Catalytic Degradation of Anthraquinones-Containing H₂O₂ Production Effluent over Layered Co-Cu Hydroxides: Defects Facilitating Hydroxyl Radicals Generation. *Appl. Catal., B* **2020**, *260*, No. 118157.
- (93) Huang, K.; Xu, Y.; Wang, L.; Wu, D. Heterogeneous Catalytic Wet Peroxide Oxidation of Simulated Phenol Wastewater by Copper Metal–Organic Frameworks. *RSC Adv.* **2015**, *5*, 32795–32803.
- (94) Giwa, A.-R. A.; Bello, I. A.; Olabintan, A. B.; Bello, O. S.; Saleh, T. A. Kinetic and Thermodynamic Studies of Fenton Oxidative Decolorization of Methylene Blue. *Heliyon* **2020**, *6*, No. e04454.
- (95) Carvalho-Silva, V. H.; Coutinho, N. D.; Aquilanti, V. Temperature Dependence of Rate Processes beyond Arrhenius and Eyring: Activation and Transitivity. *Front. Chem.* **2019**, *7*, 380.
- (96) Moumen, A.; Belhocine, Y.; Sbei, N.; Rahali, S.; Ali, F. A. M.; Mechat, F.; Hamdaoui, F.; Seydou, M. Removal of Malachite Green Dye from Aqueous Solution by Catalytic Wet Oxidation Technique Using Ni/Kaolin as Catalyst. *Molecules* **2022**, *27*, 7528.
- (97) Abdelkader, E. Heterogeneous Fenton-like Catalytic Degradation of Phenazine Dye over CeO₂ (CP-2) Nanoscale Powder. *Cerâmica* **2022**, *68*, 211–228.
- (98) Yaman, C.; Gündüz, G. A Parametric Study on the Decolorization and Mineralization of C.I. Reactive Red 141 in Water by Heterogeneous Fenton-like Oxidation over FeZSM-5 Zeolite. *J. Environ. Health Sci. Eng.* **2015**, *13*, 7.
- (99) Yang, P.; Liu, C.; Guo, Q.; Liu, Y. Variation of Activation Energy Determined by a Modified Arrhenius Approach: Roles of Dynamic Recrystallization on the Hot Deformation of Ni-Based Superalloy. *J. Mater. Sci. Technol.* **2021**, *72*, 162–171.
- (100) Almeida, L. N.; Josue, T. G.; Nogueira, O. H. L.; Ribas, L. S.; Fuziki, M. E. K.; Tusset, A. M.; Santos, O. A.; Lenzi, G. G. The Adsorptive and Photocatalytic Performance of Granite and Basalt Waste in the Discoloration of Basic Dye. *Catalysts* **2022**, *12*, 1076.
- (101) Vaiano, V.; De Marco, I. Removal of Azo Dyes from Wastewater through Heterogeneous Photocatalysis and Supercritical Water Oxidation. *Separations* **2023**, *10*, 230.
- (102) Lambert, S.; Franke, M.; Stelter, M.; Braeutigam, P. Sensing of Chemical Oxygen Demand (COD) by Amperometric Detection—Dependence of Current Signal on Concentration and Type of Organic Species. *Environ. Monit. Assess.* **2022**, *195*, 630.
- (103) Song, Y.; Xiao, M.; Li, Z.; Luo, Y.; Zhang, K.; Du, X.; Zhang, T.; Wang, Z.; Liang, H. Degradation of Antibiotics, Organic Matters and Ammonia during Secondary Wastewater Treatment Using Boron-Doped Diamond Electro-Oxidation Combined with Ceramic Ultra-filtration. *Chemosphere* **2022**, *286*, No. 131680.
- (104) Cheng, C.; Zhang, F.; Tan, M. L.; Kung, H.-T.; Shi, J.; Zhao, Q.; Wang, W.; Duan, P.; An, C.; Cai, Y.; Li, X. Characteristics of Dissolved Organic Matter and Its Relationship with Water Quality along the Downstream of the Kaidu River in China. *Water* **2022**, *14*, 3544.
- (105) Han, X.; Zhao, Y.; Zhao, F.; Wang, F.; Tian, G.; Liang, J. Novel Synthesis of Nanoscale Zero-Valent Iron from Iron Ore Tailings and Green Tea for the Removal of Methylene Blue. *Colloids Surf., A* **2023**, *656*, No. 130412.
- (106) Ma, B.; Yao, J.; Knudsen, T. Š.; Chen, Z.; Liu, B.; Zhao, C.; Zhu, X. Simultaneous Removal of Typical Flotation Reagent 8-Hydroxyquinoline and Cr (VI) through Heterogeneous Fenton-like Processes Mediated by Polydopamine Functionalized ATP Supported NZVI. *J. Hazard. Mater.* **2022**, *424*, No. 126698.
- (107) Zhao, D.; Cheng, J.; Chen, J. One-Step Synthesis of Bentonite-Supported Nanoscale Fe/Ni Bimetals for Rapid Degradation of Methyl Orange in Water. *Environ. Chem. Lett.* **2014**, *12*, 461–466.
- (108) Djebbi, M. A.; Allagui, L.; El Ayachi, M. S.; Boubakri, S.; Jaffrezic-Renault, N.; Namour, P.; Ben Haj Amara, A. Zero-Valent Iron Nanoparticles Supported on Biomass-Derived Porous Carbon for Simultaneous Detection of Cd²⁺ and Pb²⁺. *ACS Appl. Nano Mater.* **2022**, *5*, 546–558.
- (109) Ebrahiminezhad, A.; Zare-Hoseinabadi, A.; Berenjian, A.; Ghasemi, Y. Green Synthesis and Characterization of Zero-Valent Iron Nanoparticles Using Stinging Nettle (*Urtica Dioica*) Leaf Extract. *Green Processes Synth.* **2017**, *6*, 469–475.
- (110) Abdelfatah, A. M.; Fawzy, M.; Eltaweil, A. S.; El-Khouly, M. E. Green Synthesis of Nano-Zero-Valent Iron Using Ricinus Communis Seeds Extract: Characterization and Application in the Treatment of Methylene Blue-Polluted Water. *ACS Omega* **2021**, *6*, 25397–25411.
- (111) Wang, Y.; Yang, K.; Lin, D. Nanoparticulate Zero Valent Iron Interaction with Dissolved Organic Matter Impacts Iron Transformation and Organic Carbon Stability. *Environ. Sci.: Nano* **2020**, *7*, 1818–1830.
- (112) Solimeanzadeh, A.; Fekri, M.; Bakhtiary, S.; Mehrizi, M. H. Biosynthesis of Iron Nanoparticles and Their Application in Removing Phosphorus from Aqueous Solutions. *Chem. Ecol.* **2016**, *32*, 286–300.
- (113) Murgueitio, E.; Debut, A.; Landivar, J.; Cumbal, L. Synthesis of Iron Nanoparticles through Extracts of Native Fruits of Ecuador, as Capuli (*Prunus Serotina*) and Mortiño (*Vaccinium Floribundum*). *Biol. Med.* **2016**, *08*, 1.
- (114) Zhao, H.; Zhang, J.; Ye, Q.; Xu, H.; Zhou, G.; Wang, M.; Deng, W. Weak Magnetic Field Enhances the Activation of Peroxymonosulfate by ZnO@ Fe₃O₄. *RSC Adv.* **2018**, *8*, 17462–17470.
- (115) Mohagheghian, A.; Karimi, S.-A.; Yang, J.-K.; Shirzad-Siboni, M. Photocatalytic Degradation of a Textile Dye by Illuminated Tungsten Oxide Nanopowder. *J. Adv. Oxid. Technol.* **2015**, *18*, 61–68.
- (116) Hameed, A. B.; Dekhly, A. B.; Alabdrraba, W. S. Removing The Acid Orange 12 Azo Dye from Aqueous Solution Using Sodium Hypochlorite, A Kinetic and Thermodynamic Study. In *IOP Conference Series: Earth and Environmental Science*; IOP Publishing, 2022; Vol. 961, p 012056, DOI: 10.1088/1755-1315/961/1/012056.
- (117) Ghalebizade, M.; Ayati, B.; Ganjidoust, H. Capability Study of Electro-Peroxone Process in a Cylindrical Reactor in Degrading Acid Orange 7. *Linnaeus Eco-Tech* **2018**, 87–87.